Electronic noise of a single skyrmion

Kang Wang, Yiou Zhang, Vineetha Bheemarasetty, See-Chen Ying, and Gang Xiao

Phys. Rev. B **108**, 094431 — Published 22 September 2023

DOI: 10.1103/PhysRevB.108.094431

Electronic Noise of a Single Skyrmion

Kang Wang,* Yiou Zhang, Vineetha Bheemarasetty, See-Chen Ying, and Gang Xiao†
Department of Physics, Brown University, Providence, Rhode Island 02912, USA

Abstract

To enable the practical use of skyrmion-based devices, it is essential to achieve a balance between energy efficiency and thermal stability, while also ensuring reliable electrical detection against noise. Understanding how a skyrmion interacts with material disorder and external perturbations is thus essential. Here we investigate the electronic noise of a single skyrmion under the influence of thermal fluctuations and spin currents in a magnetic thin film. We detect the thermally induced noise with a $1/f^{\gamma}$ signature in the strong pinning regime but a random telegraph noise in the intermediate pinning regime. Both the thermally dominated and current-induced telegraph-like signals are detected in the weak pinning regime. Our results provide a comprehensive electronic noise picture of a single skyrmion, demonstrating the potential of noise fluctuation as a valuable tool for characterizing the pinning condition of a skyrmion. These insights could also aid in the development of low-noise and reliable skyrmion-based devices.

* kang_wang@brown.edu
† gang_xiao@brown.edu

I. INTRODUCTION

Noise fluctuation is conveniently analyzed through its power spectrum

$$S(\omega) = \left| \int_{t_1}^{t_2} x(t) e^{-i2\pi\omega t} dt \right|^2, \quad (1)$$

where $x(t)$ is the time-domain signal. The power spectrum possesses various signatures which may provide information about the nature of the dynamics. For example, a broadband $1/f^{\gamma}$ ($f = 2\pi\omega$) noise may be detected. While the noise is white when $\gamma = 0$, the $1/f^2$ signature ($\gamma = 2$) corresponds to Brownian noise and can be produced by the trajectories of a Brownian walk. According to van der Ziel's picture [1-3], the $1/f^{\gamma}$ signature may arise from a collection of non-identical random telegraph noise (RTN) oscillators with the form

$$S_x(f) = \frac{\Delta x^2}{2f_0} \frac{1}{1 + (\pi f / f_0)^2} \quad (2)$$

where f_0 is the average fluctuation rate and Δx is the difference of the quantity x between the two states. In addition to broadband noise, there may also be a narrow band noise in the detection which produces peaks at characteristic frequencies that correspond to the length scales of the system [4-8].

Noise fluctuation has proven to be a useful method for characterizing condensed matter states such as superconducting vortices [4,5,9-12], quantum fluctuations [13-18], and charge density waves [19-24]. It could be equally useful for characterizing skyrmions. Magnetic skyrmions with a fixed chirality have been observed in non-centrosymmetric bulk magnets [25-27] and magnetic multilayers [28-32] where the antisymmetric Dzyaloshinskii-Moriya interaction [33,34] (DMI) exists and favors one sense of rotation of the magnetization over the other. Magnetic skyrmions can serve as effective agents for next-generation beyond-CMOS data storage [35-38], logic [39-41], probabilistic computing [42-45], and neuromorphic computing [46] devices owing to their non-volatility, stability, and efficient controllability.

For device applications, it is necessary to manipulate a single skyrmion via spin currents [35,36,39,40,45,46], magnetic fields, or microscopic thermal fluctuations [42-45]. This must be achieved in an efficient manner while recognizing that there is a trade-off between energy efficiency and thermal stability. Furthermore, one must be able to transduce a single skyrmion into detectable electrical signals against noise. These requirements demand an understanding how a skyrmion interacts with material disorder and external perturbations. Alternatively, one may take advantage of the noise in devices such as a skyrmion true random number generator [45]. A comprehensive study of the noise properties of a skyrmion is therefore crucial and may provide fundamental guidance on how to fabricate devices that demand low-noise performance and reliable electrical detection as well as those that utilize the noise fluctuation of a skyrmion.

The noise characterization of skyrmions has been limited to particle-based models [6,47] and only recently has been studied experimentally for the motion of a skyrmion lattice in a bulk magnet with a B20 crystal structure [7,8]. It was found that the collective transport of a skyrmion lattice produces a narrow band noise with the washboard frequency corresponding to the time required for a skyrmion particle to move one period. The electronic noise of a single skyrmion, however, remains elusive. The formation of a skyrmion configuration is a result of the delicate balance between competing energies. In materials with disorder, the size and shape of a skyrmion can vary spatially [48]. The shape of the encircling domain wall around the skyrmion core is governed by the competition between “skyrmion surface” tension energy [49,50] and local pinning energy [48,51]. Additionally, external perturbations can induce spin torques on the magnetization, causing local fluctuations that generate noise in the skyrmion.

In this work, we perform a systematic study of the electronic noise produced by a single skyrmion in response to thermal fluctuations and spin currents over a wide range of pinning conditions. We detect and analyze distinct noise signatures from the thermally dominated and current-induced dynamics of a skyrmion. This study helps us understand how a skyrmion interacts with material disorder and

perturbations, which is also key to understanding the noise dynamics of other structures in physics that share similar behaviors.

II. MAGNETIC THIN FILMS AND MAGNETIC STRUCTURES

For this study, we fabricate perpendicularly magnetized multilayers of substrate/Ta/$Co_{40}Fe_{40}B_{20}$(0.95 nm)/MgO(1.6 nm)/TaO_x on thermally oxidized silicon wafers [Supplementary Note I [52]]. The magnetic configuration in this system is determined by the competition between multiple energy terms including the perpendicular magnetic anisotropy (PMA) [53-56], exchange interaction, interfacial DMI [33,34] and Zeeman energy, and can be tuned by an applied perpendicular magnetic field H_z [Supplementary Note III and Supplementary Fig. 3 [52,57,58]]. The interfacial DMI leads to chiral magnetic domain walls and stabilizes skyrmions in this system at room temperature and in a suitable field range [Supplementary Notes III and IV [52]].

We implement moderate pinning strengths by regulating the DC power (P_{Ta}) for deposition of the Ta layer [Supplementary Note V [52]]. We identify the three growth scenarios with $P_{\mathrm{Ta}} = 3, 4, \text{and } 5$ Watt as corresponding to the strong, intermediate, and weakly pinned samples, respectively [Supplementary Note V [52] and Supplementary Movies 1 – 3]. Distinct pinning conditions may result from the effects of P_{Ta} on thin-film structures and the variation in material parameters [Supplementary Note V [52], Supplementary Note V also contains Refs. [51,59-80]]. The competition between the pinning energy, thermal energy and the current determines the noise dynamics of a skyrmion, as shown in Fig. 1(a) and discussed in more detail below.

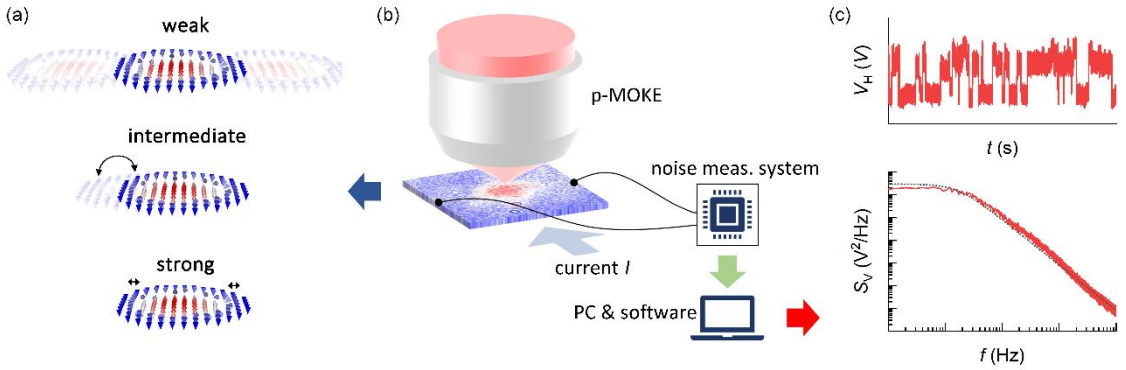

FIG. 1. Scheme of the experimental setup for studying noise of a skyrmion. (a) A schematic depiction of pinning effects on the noise dynamics of a skyrmion. In the strong pinning regime, the skyrmion is strongly pinned while multiple internal domain-wall hopping oscillations (double-headed arrows) may exist. In the intermediate pinning regime, one case is presented where one part of a skyrmion is more strongly pinned while the other part, under thermal effects, fluctuates in time between two weaker pinning sites leading to a random telegraph noise signature. In the weak pinning regime, the skyrmions hop between pinning sites more easily and both temperature and current can strongly affect the skyrmion dynamics. (b) Schematic of the experimental setup. Electronic noise of a skyrmion is studied by an electronic noise measurement system with the help of direct imaging using a polar magneto-optic Kerr effect (p-MOKE) microscope. (c) An example of the Hall voltage $V_{\mathrm{H}}(t)$ and its power spectrum $S_{\mathrm{V}}(f)$ obtained by the noise measurement system.

To study the electronic noise of a skyrmion, we nucleate a single skyrmion in a 20×20 μm^2 Hall cross and measure the magnetically induced Hall-signal fluctuations [Supplementary Note II [52,81-84] and Fig. 1(b)]. In this case, the x in Eqs. (1) and (2) is defined as the Hall voltage, $V_{\mathrm{H}} = R_{\mathrm{H}}I$, where R_{H} is the Hall resistance. Notably, R_{H} is dominated by the anomalous Hall resistance that is proportional to the perpendicular magnetization, while the conventional Hall resistance proportional to H_{z} can be neglected in comparison [85]. We measure the noise under an applied current I and a perpendicular magnetic field H_{z}. The electric current is converted into a spin current through the spin Hall solid, Ta, which exerts spin-orbit torques on the skyrmion [86-88]. This study provides us with both amplitude and frequency details of the noise of a skyrmion in responses to the external perturbations.

III. ELECTRONIC NOISE OF A SKYRMION IN DIFFERENT PINNING REGIMES

We summarize in Fig. 2 the electronic noise results of a single skyrmion in the strong, intermediate, and weak pinning regimes. All results are measured in the temperature range from 298.9 to 319.5 K and in the current range from 0.01 to 1.0 mA. As described in more detail below, we detect a thermally induced noise with a $1/f^{\gamma}$ signature in the strong pinning regime [Fig. 3] but a RTN in the intermediate pinning regime [Fig. 4]. Both the thermally dominated and current-induced telegraph-like signals are detected in the weak pinning regime [Fig. 5].

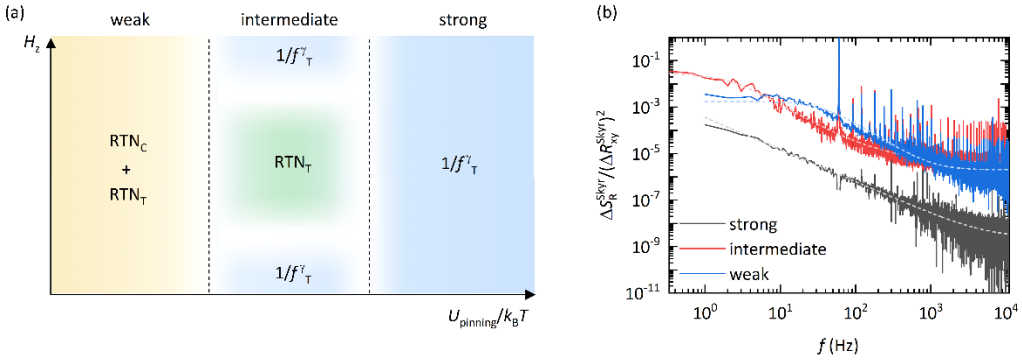

FIG. 2. (a) Summary of electronic noise of a skyrmion

n in different pinning regimes. The subscripts "T" and "C" represent the noise of thermally dominated or current-induced dynamics, respectively. We detect a thermally induced noise with a $1/f^{\gamma}$ signature in the strong pinning regime but a RTN in the intermediate pinning regime. Both the thermally induced and current-induced telegraph-like signals are detected in the weak pinning regime. (b) Normalized Hall-resistance noise $\Delta S_{\mathrm{R}}^{\mathrm{Skyr}}/\left(\Delta R_{\mathrm{xy}}^{\mathrm{Skyr}}\right)^2$ of a skyrmion in different pinning regimes. $\Delta R_{\mathrm{xy}}^{\mathrm{Skyr}}$ and $\Delta S_{\mathrm{R}}^{\mathrm{Skyr}}$ represent average contributions of each skyrmion to the anomalous Hall resistance and Hall-resistance noise, respectively. In the intermediate and weak pinning regimes, we make the approximation that $\Delta S_{\mathrm{R}}^{\mathrm{Skyr}} \approx S_{\mathrm{R}}$ for $N_{\mathrm{Skyr}} = 1$. This is justified as the S_{R} for $N_{\mathrm{Skyr}} = 1$ significantly exceeds the background noise level, which can be disregarded in our calculations.

Figure 2(b) summarizes the amplitude details of the noise of a skyrmion for each pinning region. Instead of presenting noise S_{R}, we present a normalized Hall-resistance noise $\Delta S_{\mathrm{R}}^{\mathrm{Skyr}}/\left(\Delta R_{\mathrm{xy}}^{\mathrm{Skyr}}\right)^2$ where $\Delta R_{\mathrm{xy}}^{\mathrm{Skyr}}$ and $\Delta S_{\mathrm{R}}^{\mathrm{Skyr}}$ are average contributions of each skyrmion to the anomalous Hall resistance and Hall-resistance noise, respectively, as discussed below. The normalized noise accounts for the variations in the Hall resistance of a single skyrmion across different samples and therefore allows us to compare different samples.

A. $1/f^{\gamma}$ noise of a skyrmion in the strong pinning regime

In the strong pinning regime, skyrmions move negligibly owing to the lower thermal energy relative to the pinning energy U_{pinning}. Still, the internal domain-wall hopping exists and may contribute to the $1/f^{\gamma}$ noise signature [Fig. 3(b), also see Supplementary Note VI and Supplementary Figs. 7 and 8 [52], Supplementary Note VI also contains Refs. [89-91]]. The speculation of internal domain-wall hopping oscillations contributing to the $1/f^{\gamma}$ noise of a skyrmion finds validation through micromagnetic simulations as depicted in Supplementary Note VII and Supplementary Fig. 9 [52] [Supplementary Note VII also contains Refs. [92]]. The pinning energy U_{pinning} governs the domain-wall hopping through the Arrhenius law $f_0 = f_{00}\exp\left(-U_{\mathrm{pinning}}/k_{\mathrm{B}}T\right)$, where f_{00} is the attempt frequency. The U_{pinning} distribution therefore affects the distribution of the internal domain-wall hopping oscillators as well as the noise signature from this collection of non-identical oscillators. Conversely, the distribution of U_{pinning} can be inferred through an examination of the noise spectrum. When the distribution is uniform, the value of γ equals 1. A fitting of the $1/f^{\gamma}$ noise with $\gamma = 1.36$ [gray curve in Fig. 3(b)] uncovers the U_{pinning} distribution contributing to the $1/f^{\gamma}$ noise, as depicted in Fig. 3(a). For further fitting specifics, refer to Supplementary Note VIII [52] [Supplementary Note VIII also contains Refs. [77,93-95]].

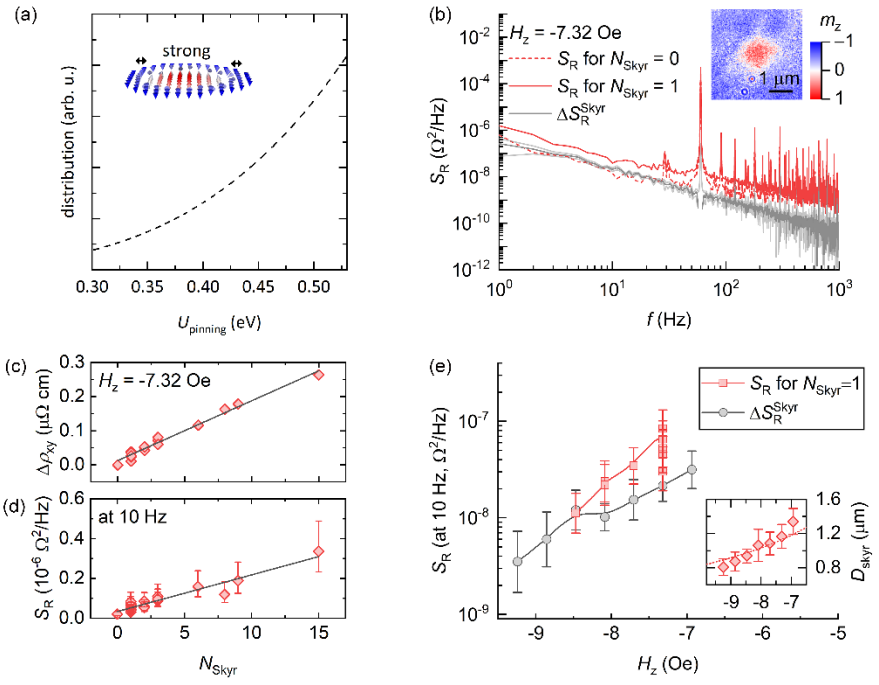

FIG. 3. $1/f^{\gamma}$ noise of a skyrmion in the strong pinning regime. (a) A plot illustrating distribution of the U_{pinning} that contribute to the $1/f^{\gamma}$ noise of a skyrmion. The result is obtained by fitting the gray curve in (b), which exhibits a $1/f^{\gamma}$ signature with $\gamma = 1.36$. The inset provides a schematic depiction of the noise dynamics of a skyrmion under strong pinning, where the skyrmion is strongly immobilized while potentially undergoing multiple internal domain-wall hopping oscillations (double-headed arrows). (b) Red dashed line: S_{R} spectra with the $1/f^{\gamma}$ noise signature for $N_{\text{Skyr}} = 0$ at $H_{\text{z}} = -7.32$ Oe. Red solid line: S_{R} spectra with the $1/f^{\gamma}$ noise signature for $N_{\text{Skyr}} = 1$ at $H_{\text{z}} = -7.32$ Oe. Gray line: an average contribution of each skyrmion to the noise $\Delta S_{\text{R}}^{\text{Skyr}}$ where the background noise is subtracted. The inset shows a p-MOKE image of the skyrmion for noise measurements. (c) The relative Hall resistivity $\Delta\rho_{\text{xy}}$ as a function of N_{Skyr}. (d) S_{R} at 10 Hz as a function of N_{Skyr}. The dotted line is a linear fit to $S_{\text{R}} = S_{\text{R},0} + \Delta S_{\text{R}}^{\text{Skyr}} N_{\text{Skyr}}$. (e) S_{R} for $N_{\text{Skyr}} = 1$, $\Delta S_{\text{R}}^{\text{Skyr}}$ and the skyrmion diameter D_{Skyr} as a function of H_{z}. Dotted line in the inset represents the fit to the experimental data using a theoretical model [96] [Supplementary Note II [45,52,88,96]].

To eliminate the background noise, we study the noise of discrete skyrmions at a constant field [Supplementary Note VI and Supplementary Fig. 7 [52]]. At a field where skyrmions are stabilized, multiple states with variable skyrmion numbers N_{Skyr} may be accessed through a field cycling process

[Supplementary Note IV [52]]. Figure 3(c) shows a linear variation of the relative Hall resistivity $\Delta\rho_{xy}$ with N_{Skyr}. Each skyrmion contributes to the $\Delta\rho_{xy}$ in the amount of $\Delta\rho_{xy}^{Skyr} = 17.6 \pm 1.25$ nΩ cm. This aligns closely with the previously reported electrical detection of an isolated skyrmion using the anomalous Hall effect [97]. In addition, the Hall-resistance noise S_R also increases linearly with N_{Skyr} [Fig. 3(d)]. Fitting to $S_R = S_{R,0} + \Delta S_R^{Skyr} N_{Skyr}$ yields the average contribution of each skyrmion to the noise ΔS_R^{Skyr} as well as the contribution from the uniform magnetization state $S_{R,0}$. This fitting assumes negligible interactions between skyrmions due to their large spatial separation [Supplementary Note VI [52]]. Although ΔS_R^{Skyr} is smaller than the background noise by one order of magnitude [Supplementary Fig. 7 [52]], it is distinguishable and clearly exhibits the $1/f^{\gamma}$ signature [gray line in Fig. 3(b)]. Analogous measurements performed at different fields for this sample and other samples all concur with the $1/f^{\gamma}$ signature with $1.0 < \gamma < 1.4$, independent of the skyrmion's polarization [Supplementary Note VI and Supplementary Fig. 8 [52]].

B. Field-dependent $1/f^{\gamma}$ noise of a skyrmion

Figure 3(e) displays the field-dependent noise of a skyrmion at 10 Hz as well as the skyrmion diameter D_{Skyr}. It is noted that while the skyrmion size decreases by about 43% from −6.93 to −9.24 Oe [inset in Fig. 3(e)], the ΔS_R^{Skyr} decreases by almost two orders of magnitude. This is contrary to what one would expect, which is that the number of internal domain-wall hopping oscillators is proportional to the total length of domain walls which would thereby linearly affect the noise amplitude [Supplementary Note IX and Supplementary Fig. 10 [52]]. The significant reduction in noise with respect to the skyrmion size suggests that the number of internal domain-wall hopping oscillators in a skyrmion decreases significantly with a reduction in skyrmion size. It can be inferred that smaller skyrmions are more appropriate for applications due to their substantially lower noise levels.

We calculate the signal-to-noise ratio (SNR) by using $\sqrt{\Delta S_{\mathrm{R}}^{\mathrm{Skyr}}}/\Delta R_{\mathrm{xy}}^{\mathrm{Skyr}}$ where $\Delta R_{\mathrm{xy}}^{\mathrm{Skyr}}$ is the average contribution of each skyrmion to the anomalous Hall resistance. The SNR of a skyrmion is on the order of 2.0% $\mathrm{Hz}^{-0.5}$ at 1 Hz and 0.5% $\mathrm{Hz}^{-0.5}$ at 10 Hz, as evidenced by $\mathrm{SNR}^2 = \Delta S_{\mathrm{R}}^{\mathrm{Skyr}}/\left(\Delta R_{\mathrm{xy}}^{\mathrm{Skyr}}\right)^2$ in Fig. 2(b). A low SNR is crucial in the electrical detection of a skyrmion owing to the small signal from this tiny magnetic structure [46,97].

C. Random telegraph noise of a skyrmion in the intermediate pinning regime

In the intermediate pinning regime, a skyrmion exhibits the ability to hop between certain pinning sites with greater ease yet remains strongly pinned by specific pinning centers. [Supplementary Note X, Supplementary Fig. 11 [52], and Supplementary Movie 4]. The case presented here involves one part of a skyrmion being more strongly pinned while the other part, under thermal effects, fluctuates in time between two weaker pinning sites [Figs. 4(a) and (b)]. This behavior is schematically represented by the bended double-headed arrow in Fig. 4(a). This produces a RTN signature [Fig. 4(c), also see Ref. [45]]. Along with the RTN, we identify a fluctuation in $\Delta\rho_{\mathrm{xy}}$ over time between two discrete states and correspondingly a skyrmion-size variation between a small-skyrmion ($\Delta\rho_{\mathrm{xy}} \approx 0$) and a large-skyrmion ($\Delta\rho_{\mathrm{xy}} \approx 8$ nΩ cm) configuration [Fig. 4(d) and Supplementary Movie 5]. This shares the same physics as the internal domain-wall hopping oscillations in the strong pinning regime. There may also be more internal domain-wall hopping oscillations in the skyrmion, depicted by the straight double-headed arrow in Fig. 4(a). Nevertheless, these oscillations manifest with significantly smaller amplitudes $\Delta {V_{\mathrm{H}}}^2/2I^2$. Their contributions to the overall noise [$10^{-7} - 10^{-6}\ \Omega^2/\mathrm{Hz}$ at 1 Hz as shown by the gray curve in Fig. 4(c)] are negligible in comparison to the detected noise in the intermediate pinning regime [$10^{-5}\ \Omega^2/\mathrm{Hz}$ at 1 Hz as shown by the red curve in Fig. 4(c)].

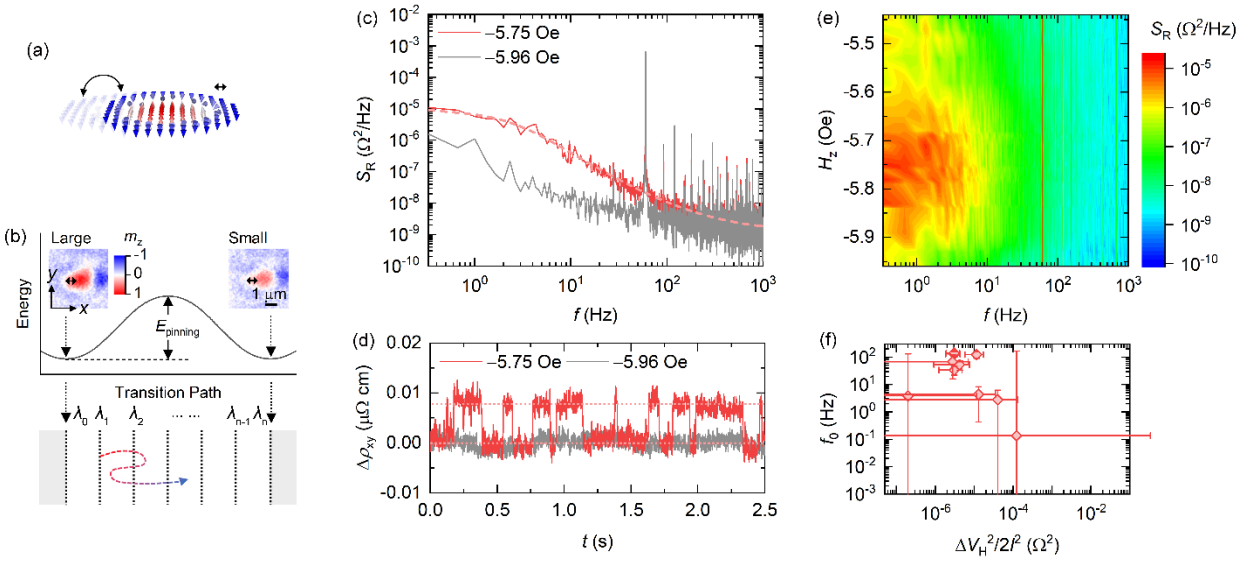

FIG. 4. Random telegraph noise of a skyrmion in the intermediate pinning regime. (a) Schematic depiction of skyrmion dynamics in the intermediate pinning regime. The case presented here involves one part of a skyrmion being more strongly pinned while the other part, under thermal effects, fluctuates in time between two weaker pinning sites leading to a random telegraph noise signature. (b) Energy path for the two-state transition. The small-skyrmion and large-skyrmion states occur at local minima in the energy landscape separated by an energy barrier. The transition between the two states involves passing through a series of interfaces, $\{\lambda_{\mathrm{L}} = \lambda_0, \lambda_1, \cdots, \lambda_{\mathrm{n}-1}, \lambda_{\mathrm{n}} = \lambda_{\mathrm{S}}\}$, defined as isosurfaces of a monotonically varying order parameter, ζ, such as the perpendicular magnetization m_{z}. Due to the presence of thermal energy, recrossings between neighboring interfaces are inevitable, as illustrated by the dashed arrow in the schematic. (c) Hall-resistance noise spectra S_{R} of a skyrmion in the intermediate pinning regime. The spectra are measured at $H_{\mathrm{z}} = -5.75$ Oe (red) and -5.96 Oe (gray) where the skyrmion fluctuates in time between the two states or remains in a deterministic small-skyrmion state, respectively. The dashed line is a fit to the RTN plus a $1/f^{\gamma}$ noise. (d) Relative Hall-resistivity $\Delta\rho_{\mathrm{xy}}$ variations in time of a skyrmion at $H_{\mathrm{z}} = -5.75$ Oe (red) and -5.96 Oe (gray). (e) Map of Hall-resistance noise spectra S_{R} at different fields. A transition of the RTN into the $1/f^{\gamma}$ noise is observed by increasing or decreasing the field to the deterministic small-skyrmion and large-skyrmion state, respectively. (f) The fluctuation rate f_0 as a function of the amplitude $\Delta V^2/2I^2$ of the RTN of isolated skyrmions in the intermediate pinning regime. All results are measured at 307.1 K and with a current $I = -0.2$ mA. This current corresponds to the current density of -2.4×10^9 A/m^2 flowing in the Ta buffer layer. The red curve in (d) is reproduced from Ref. [45].

The two identified states, referred to as the "small-skyrmion" and "large-skyrmion" states, correspond to local minima in the energy landscape, separated by an energy barrier, as illustrated in Fig. 4(b). The fluctuation between these states is thermally induced, and the fluctuation rate is determined by the competition between the pinning energy barrier U_{pinning} and the thermal energy $k_{\mathrm{B}}T$. Our previous work has shown that the energy landscape can be influenced by adjusting the applied magnetic field and a spin current through the Zeeman energy and spin-orbit torques, respectively [45]. This enables the manipulation of the local dynamics of a skyrmion and, in turn, influences the noise generated by the system [45]. The skyrmion is more likely being in the small-skyrmion state when the applied field H_{z} is increased or when the current is applied along the $+x$ axis in Fig. 4(b) [45]. Similarly, the large-skyrmion state is more probable with decreasing the applied field or applying a current in the $-x$ axis [45]. Along with the deterministic small-skyrmion and large-skyrmion configuration at a higher or lower field, respectively, a $1/f^{\gamma}$ noise signature is detected [Figs. 4(c) and (e)]. This closely resembles the behavior of a strongly pinned skyrmion.

D. Effects of the energy landscape on the internal domain-wall hopping oscillation dynamics

We observe and analyze the RTN for multiple isolated skyrmions where the fluctuation rate f_0 varies between skyrmions [Fig. 4(f), also see Supplementary Note X and Supplementary Fig. 12 [52]]. This fluctuation rate variation is a result of different energy paths for the two-state transition and provides us with a platform to study how the energy landscape affects the internal domain-wall hopping oscillation dynamics of a skyrmion. The Arrhenius law $f_0 = f_{00}\exp\left(-U_{\mathrm{pinning}}/k_{\mathrm{B}}T\right)$ tells us how U_{pinning} and the thermal energy $k_{\mathrm{B}}T$ affect the RTN dynamics. Additionally, the attempt frequency f_{00} may carry an activation entropy which implies that a longer path must be explored more randomly [98-100]. It has been identified recently through simulation studies that the entropic effect is crucial in describing other processes including the magnetization switching [98,100] and skyrmion annihilation [99]. The entropic effect can be elucidated through the forward flux sampling method, which involves a series of interfaces

$\{\lambda_0 = \lambda_{\mathrm{L}}, \lambda_1, \cdots, \lambda_{\mathrm{n}-1}, \lambda_{\mathrm{n}} = \lambda_{\mathrm{S}}\}$ in configuration space between the large-skyrmion and small-skyrmion states. These interfaces are defined as isosurfaces of a monotonically varying order parameter, ζ, such as the perpendicular magnetization m_{z} [Fig. 4(b)]. Despite the energy profile being characterized by two local minima and an energy barrier in between, recrossings between neighboring interfaces are inevitable owing to the thermal energy. The fluctuation rate is then expressed as $\prod_{i=0}^{\mathrm{n}-1} P(\lambda_{i+1}|\lambda_i)$, where $P(\lambda_{i+1}|\lambda_i)$ represents the probability that a trajectory originating from λ_i reaching λ_{i+1} before returning to the basin initial state. For a large skyrmion-size variation, more interfaces are required to transition from the basin large-skyrmion to the small-skyrmion state, reducing $\prod_{i=0}^{\mathrm{n}-1} P(\lambda_{i+1}|\lambda_i)$ and, consequently, the fluctuation rate. We illustrate in Fig. 4(e) that f_0 increases when decreasing $\Delta {V_{\mathrm{H}}}^2/2I^2$, with $\Delta {V_{\mathrm{H}}}^2/2I^2$ reflecting the skyrmion-size variation. This provides evidence that, in addition to the U_{pinning} and thermal energy $k_{\mathrm{B}}T$, the entropic effect is also crucial in the noise dynamics of a skyrmion.

We note that the RTN transitions into the $1/f^{\gamma}$ noise by increasing N_{Skyr} [Supplementary Note X and Supplementary Fig. 13 [52]]. Each skyrmion represents a RTN oscillator. A collection of multiple skyrmions represents a system that verifies the $1/f^{\gamma}$ signature arising from a collection of multiple internal domain-wall hopping oscillators.

E. Thermally induced and current-induced telegraph-like noise in the weak pinning regime

In the weak pinning regime, skyrmions exhibit enhanced mobility as they readily hop between pinning sites [Fig. 5(a), also see Supplementary Movie 2 and Supplementary Fig. 3 [52]]. In this scenario, we are unable to detect the electronic noise of a specified skyrmion. In addition to the thermal fluctuation, the current may also play a significant role in the dynamics.

In this section, we begin with displaying the S_{R} measured at $H_{\mathrm{z}} = -3.58$ Oe where multiple skyrmions are stabilized [Supplementary Movie 6] to illustrate the noise signature and underlying physics [Figs. 5(b) – (e)]. It is observed that skyrmions fit commensurably into the Hall cross at this field.

However, this commensurability effect is not observed in the strong and intermediate pinning regimes, where the skyrmion order is constrained by the pinning sites.

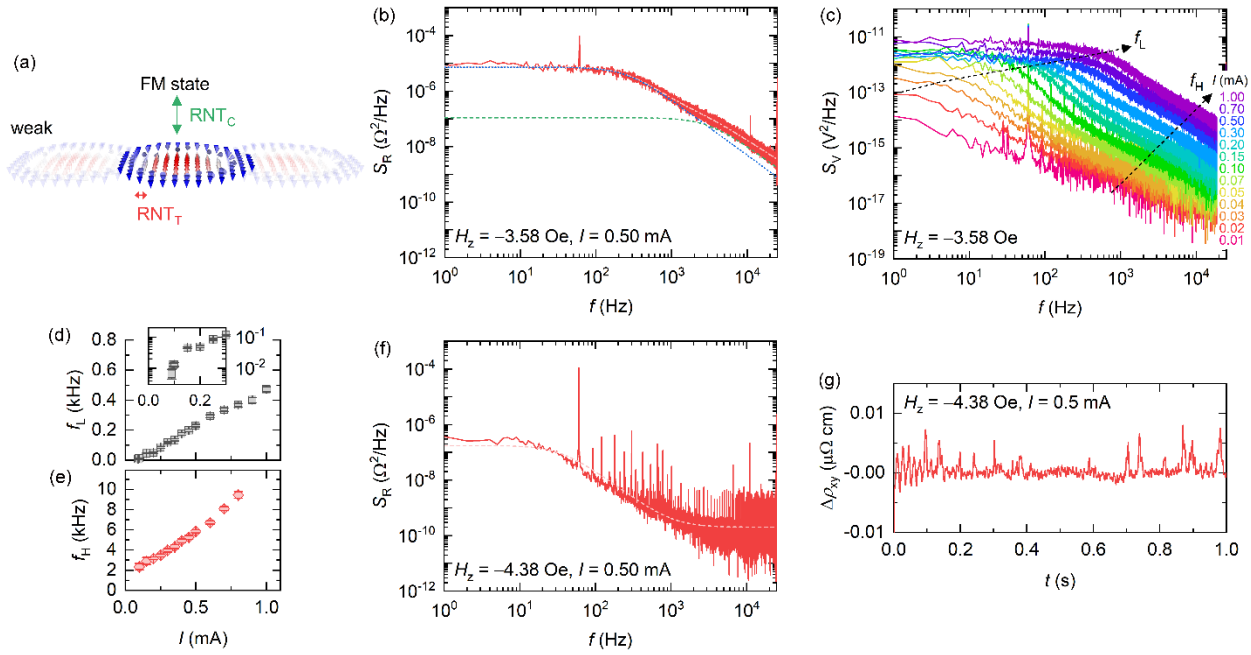

FIG. 5. Thermally induced and current-induced telegraph-like noise of a skyrmion in the weak pinning regime. (a) Schematic depiction of the skyrmion dynamics in the weak pinning regime. Skyrmions exhibit enhanced mobility as they readily hop between pinning sites. Both temperature and current can strongly affect the skyrmion dynamics. (b) Hall-resistance noise S_{R} measured at $H_{\mathrm{z}} = -3.58$ Oe where skyrmions are stabilized. The dash-dotted line is a fit to Eq. (3). The dotted blue and dashed green lines are fits to the lower-frequency and higher-frequency telegraph-like noise, respectively. (c) Hall-voltage noise S_{V} measured at various currents. (d), (e) The central frequency f_{L} (d) and f_{H} (e) of the lower-frequency and higher-frequency telegraph-like noise as a function of current I. The inset in (d) presents a semi-logarithmic plot to highlight the low current range. 1 mA current corresponds to the current density of 1.2×10^{10} A/m^2 flowing in the Ta buffer layer. (f) Hall-resistance noise S_{R} measured at $H_{\mathrm{z}} = -4.38$ Oe. (g) relative Hall-resistivity $\Delta\rho_{\mathrm{xy}}$ variations in time at $H_{\mathrm{z}} = -4.38$ Oe where only a single skyrmion may be nucleated. Nucleation of a skyrmion leads to an increase in $\Delta\rho_{\mathrm{xy}}$ which reduces back to zero when the skyrmion propagates out of the Hall cross. All results are measured at 319.5 K.

We observe two telegraph-like noise signals in Fig. 5(b) which can be well fitted to,

$$S_{\mathrm{V}} = \frac{S_{\mathrm{V},0}^{1\mathrm{Hz}}}{f^{\gamma}} + \frac{\Delta {V_{\mathrm{H,L}}}^2/2f_{\mathrm{L}}}{1+(\pi f/f_{\mathrm{L}})^2} + \frac{\Delta {V_{\mathrm{H,H}}}^2/2f_{\mathrm{H}}}{1+(\pi f/f_{\mathrm{H}})^2}, \quad (3)$$

where $\Delta {V_{\mathrm{H,L}}}^2/2I^2$ and $\Delta {V_{\mathrm{H,H}}}^2/2I^2$ are amplitudes of the lower-frequency and the higher-frequency telegraph-like signals, respectively. In our classification, we refer to this noise as "telegraph-like noise" instead of "RTN" because it arises from a collection of multiple internal domain-wall hopping RTN oscillators, though with a narrow distribution of these oscillators, as elaborated upon below. Notably, we confirm that the lower-frequency signal originates from the current effect as the central frequency f_{L} decreases and approaches zero when the current is decreased to zero [Figs. 5(c) and (d)]. The higher-frequency signal is dominated by the thermal effect since the central frequency f_{H} approaches a non-zero value (approximately 2 kHz) in the zero-current limit [Figs. 5(c) and (e)]. We note that the temperature induced by Joule heating, over the range of currents employed in our study, remain below 1 K [Supplementary Note XI and Supplementary Fig. 14 [52]], which is negligible in comparison to the range of temperatures under our investigation.

When the magnetic field is increased to $H_{\mathrm{z}} = -4.38$ Oe, Hall-resistance measurements in Fig. 5(g) show that only discrete skyrmions are nucleated and annihilated by the current, as evidenced by distinct spikes. As a result, the lower-frequency RTN is visible, while the higher-frequency signal dominated by thermal effects is suppressed. These observations suggest that the lower-frequency RTN arises from the current-induced skyrmion nucleation and annihilation process, which is discussed in further detail below.

We investigate the origins of the two noise signals by probing Hall-voltage fluctuations over a smaller Hall cross with dimensions of 5×5 μm^2, where only a single magnetic bubble can be nucleated and propagate [inset in Fig. 6(a)]. We cannot ascertain whether the magnetic bubbles are topologically equivalent to skyrmions or not. To avoid any misleading, we refer to them as "magnetic bubbles" rather than "skyrmions". However, this distinction does not impact our understanding of the origins of the two

noise signals. We nucleate a magnetic bubble at defect positions or at sample boundaries. At a small current (≤ 0.06 mA), the magnetic bubble domain is elongated and flows continuously through the Hall cross and only the higher-frequency telegraph-like noise is visible [Fig. 6(a)]. By contrast, a larger current (≥ 0.07 mA) induces discrete domain nucleation and propagation, causing the Hall voltage to fluctuate in time between two discrete states [inset in Fig. 6(b), also see Supplementary Movie 7]. This thereby results in the additional lower-frequency bump [Figs. 6(a) and (b)]. The power spectrum over a period from 0.15 to 0.22 s of the Hall signal, again, only shows the higher-frequency signal [gray line in Fig. 6(b)]. During this time, a domain continuously flows through the Hall cross. These results indicate that the lower-frequency telegraph noise is a result of current-induced bubble domain nucleation and propagation while the higher-frequency signal most likely arises from thermally dominated domain-wall fluctuations, as it is visible even with only a single bubble domain propagating through the Hall cross and has not been observed in the saturated ferromagnetic state. In the weak pinning regime, U_{pinning} exhibits a much narrower distribution. This results in the telegraph-like noise signature [Figs. 5(b) and (c), and Figs. 6(a) and (b)], in contrast to $1/f^{\gamma}$ noise signature in the strong pinning regime, with the measured frequency f_{H} being the averaged result over the domain-wall hopping oscillation dynamics.

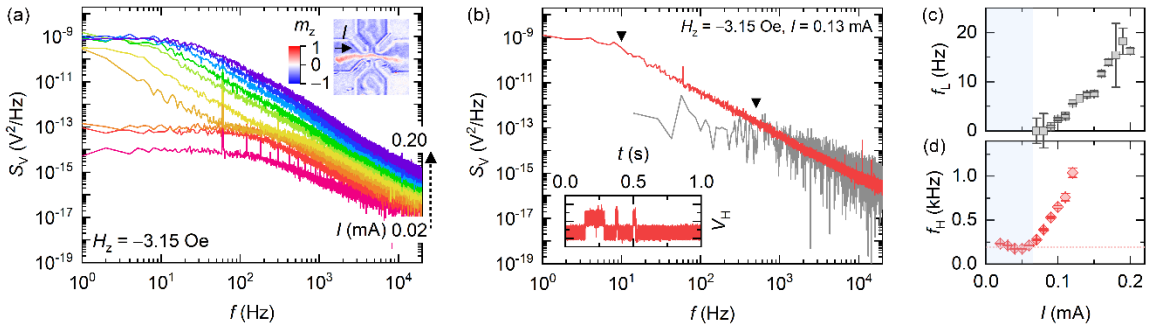

FIG. 6. Electronic noise of a bubble domain in a Hall cross with a dimension of 5×5 μm^2. (a) Hall-voltage noise S_{V} measured at various currents. The inset shows a p-MOKE image of the Hall cross with a dimension of 5×5 μm^2 where only a single elongated magnetic bubble is nucleated and propagates through the Hall cross. (b) S_{V} measured at $I = 0.13$ mA. The inset shows the Hall-voltage variations in time at $I = 0.13$ mA. The gray line is the power

spectral density of the period between 0.15 and 0.22 s of Hall-voltage signals. (c), (d) The central frequency f_{L} (c) and f_{H} (d) of the lower-frequency and higher-frequency telegraph-like noise as a function of current I. All results are measured at 318.3 K. In this configuration, a current of 1 mA corresponds to a current density of 4.8×10^{10} A/m^2 flowing in the underlying Ta buffer layer.

IV. DISCUSSION AND CONCLUSION

Our work has revealed comprehensive electronic noise properties of a single skyrmion. Distinctive amplitudes and frequency spectra can be mapped out according to the strong, intermediate, and weak pinning regimes. As summarized in Fig. 2, we detect a noise with a $1/f^{\gamma}$ signature in the strong pinning regime but a RTN in the intermediate pinning regime, and two telegraph-like signals in the weak pinning regime. Distinct noise signatures arise from the thermally dominated internal domain-wall hopping oscillation and/or the current-induced skyrmion nucleation. It is understood that the competition between the thermal and pinning energies governs the internal domain-wall hopping oscillation dynamics. Additionally, we reveal that the entropic effect is also significant in determining the dynamics and thereby the resulting noise signatures.

Our results demonstrate that noise fluctuation can serve as an insightful probe for characterizing the pinning condition of a skyrmion, with the $1/f^{\gamma}$ signature indicating a flatter distribution of oscillators in the strong pinning regime [Fig. 3(a)]. In contrast, a much narrower distribution leads to telegraph-like noise in the weak pinning regime.

Furthermore, our research has implications for applications that either require reliable electrical detection or utilize the inherent noise of a skyrmion. A comprehensive noise picture of a skyrmion can guide the fabrication of low-noise and reliable skyrmion-based devices. In the strong and intermediate pinning regimes, the skyrmion exhibits high thermal stability, but pinning effects impede its efficient manipulation. In contrast, a skyrmion can be efficiently manipulated in the weak pinning regime, although its thermal stability is reduced. We note that even a small current of 6.1×10^9 A/m^2 may cause

the unwanted nucleation of a skyrmion [Figs. 5(f) and (g)], which may impose a current limit for applications. Alternatively, artificial pinning centers may be used to guide a skyrmion along a desirable path and position it at a fixed location for detection. In this way, artificial pinning centers can help to achieve the trade-off between energy efficiency and thermal stability necessary for applications. Noise fluctuation can also be an insightful probe for characterizing skyrmion interactions with artificial pinning.

Additionally, our noise study of a skyrmion may also be key to understanding the noise dynamics of other structures such as superconducting vortices [10] and charge density waves [23] that exhibit similar behaviors [Supplementary Note XII [52]]. A complete picture connecting the noise and the dynamics of these condensed matter states remains elusive and demands further exploration.

ACKNOWLEDGEMENTS

G.X. acknowledges funding support from the National Science Foundation (NSF) under Grant No. OMA-1936221. Y.Z. acknowledges funding support from the Fermilab-Graduate Instrumentation Research Award from DOE Award No. DE-AC05-00OR22725. We use the Heidelberg MLA150 maskless aligner which is under the support of NSF Grant No. DMR-1827453.

REFERENCES

[1] A. Van Der Ziel, On the noise spectra of semi-conductor noise and of flicker effect, Physica **16**, 359 (1950).

[2] M. Weissman, 1 f noise and other slow, nonexponential kinetics in condensed matter, Rev. Mod. Phys. **60**, 537 (1988).

[3] P. Dutta and P. Horn, Low-frequency fluctuations in solids: 1 f noise, Rev. Mod. Phys. **53**, 497 (1981).

[4] G. D'anna, P. Gammel, H. Safar, G. Alers, D. Bishop, J. Giapintzakis, and D. Ginsberg, Vortex-motion-induced voltage noise in YBa 2 Cu 3 O 7− δ single crystals, Phys. Rev. Lett. **75**, 3521 (1995).

[5] Y. Togawa, R. Abiru, K. Iwaya, H. Kitano, and A. Maeda, Direct Observation of the Washboard Noise of a Driven Vortex Lattice in a High-Temperature Superconductor, Bi 2 Sr 2 CaCu 2 O y, Phys. Rev. Lett. **85**, 3716 (2000).

[6] S. A. Díaz, C. O. Reichhardt, D. P. Arovas, A. Saxena, and C. Reichhardt, Fluctuations and noise signatures of driven magnetic skyrmions, Phys. Rev. B **96**, 085106 (2017).

[7] T. Sato, W. Koshibae, A. Kikkawa, T. Yokouchi, H. Oike, Y. Taguchi, N. Nagaosa, Y. Tokura, and F. Kagawa, Slow steady flow of a skyrmion lattice in a confined geometry probed by narrow-band resistance noise, Phys. Rev. B **100**, 094410 (2019).

[8] T. Sato, A. Kikkawa, Y. Taguchi, Y. Tokura, and F. Kagawa, Mode locking phenomena of the current-induced skyrmion-lattice motion in microfabricated MnSi, Phys. Rev. B **102**, 180411 (2020).

[9] S. Okuma, J. Inoue, and N. Kokubo, Suppression of broadband noise at mode locking in driven vortex matter, Phys. Rev. B **76**, 172503 (2007).

[10] A. Marley, M. Higgins, and S. Bhattacharya, Flux flow noise and dynamical transitions in a flux line lattice, Phys. Rev. Lett. **74**, 3029 (1995).

[11] C. Olson, C. Reichhardt, and F. Nori, Nonequilibrium dynamic phase diagram for vortex lattices, Phys. Rev. Lett. **81**, 3757 (1998).

[12] T. Tsuboi, T. Hanaguri, and A. Maeda, Local Density Fluctuations of Moving Vortices in the Solid and Liquid Phases in Bi 2 Sr 2 CaCu 2 O y, Phys. Rev. Lett. **80**, 4550 (1998).

[13] J. M. Martinis, S. Nam, J. Aumentado, and C. Urbina, Rabi oscillations in a large Josephson-junction qubit, Phys. Rev. Lett. **89**, 117901 (2002).

[14] E. Paladino, Y. Galperin, G. Falci, and B. Altshuler, 1/f noise: Implications for solid-state quantum information, Rev. Mod. Phys. **86**, 361 (2014).

[15] O. S. Lumbroso, L. Simine, A. Nitzan, D. Segal, and O. Tal, Electronic noise due to temperature differences in atomic-scale junctions, Nature **562**, 240 (2018).

[16] Y. Zhang and G. Xiao, Spin-dependent shot noise in MgO-based magnetic tunnel junctions under noncollinear magnetization alignment, Phys. Rev. B **100**, 224402 (2019).

[17] S. Larocque, E. Pinsolle, C. Lupien, and B. Reulet, Shot noise of a temperature-biased tunnel junction, Phys. Rev. Lett. **125**, 106801 (2020).

[18] O. Shein-Lumbroso, J. Liu, A. Shastry, D. Segal, and O. Tal, Quantum flicker noise in atomic and molecular junctions, Phys. Rev. Lett. **128**, 237701 (2022).

[19] R. Fleming and C. Grimes, Sliding-Mode Conductivity in Nb Se 3: Observation of a Threshold Electric Field and Conduction Noise, Phys. Rev. Lett. **42**, 1423 (1979).

[20] G. Grüner, A. Zawadowski, and P. Chaikin, Nonlinear conductivity and noise due to charge-density-wave depinning in nb se 3, Phys. Rev. Lett. **46**, 511 (1981).

[21] I. Bloom, A. Marley, and M. Weissman, Nonequilibrium dynamics of discrete fluctuators in charge-density waves in NbSe 3, Phys. Rev. Lett. **71**, 4385 (1993).

[22] K. Bennaceur, C. Lupien, B. Reulet, G. Gervais, L. Pfeiffer, and K. West, Competing charge density waves probed by nonlinear transport and noise in the second and third Landau levels, Phys. Rev. Lett. **120**, 136801 (2018).

[23] M. Yoshida, T. Sato, F. Kagawa, and Y. Iwasa, Charge density wave dynamics in nonvolatile current-induced phase transition in 1 T− Ta S 2, Phys. Rev. B **100**, 155125 (2019).

[24] A. K. Geremew, S. Rumyantsev, B. Debnath, R. K. Lake, and A. A. Balandin, High-frequency current oscillations in charge-density-wave 1T-TaS2 devices: Revisiting the "narrow band noise" concept, Appl. Phys. Lett. **116**, 163101 (2020).

[25] S. Mühlbauer, B. Binz, F. Jonietz, C. Pfleiderer, A. Rosch, A. Neubauer, R. Georgii, and P. Böni, Skyrmion lattice in a chiral magnet, Science **323**, 915 (2009).

[26] X. Yu, Y. Onose, N. Kanazawa, J. H. Park, J. Han, Y. Matsui, N. Nagaosa, and Y. Tokura, Real-space observation of a two-dimensional skyrmion crystal, Nature **465**, 901 (2010).

[27] X. Yu, N. Kanazawa, Y. Onose, K. Kimoto, W. Zhang, S. Ishiwata, Y. Matsui, and Y. Tokura, Near room-temperature formation of a skyrmion crystal in thin-films of the helimagnet FeGe, Nat. Mater. **10**, 106 (2011).

[28] N. Romming, C. Hanneken, M. Menzel, J. E. Bickel, B. Wolter, K. von Bergmann, A. Kubetzka, and R. Wiesendanger, Writing and deleting single magnetic skyrmions, Science **341**, 636 (2013).

[29] W. Jiang, P. Upadhyaya, W. Zhang, G. Yu, M. B. Jungfleisch, F. Y. Fradin, J. E. Pearson, Y. Tserkovnyak, K. L. Wang, and O. Heinonen, Blowing magnetic skyrmion bubbles, Science **349**, 283 (2015).

[30] C. Moreau-Luchaire, C. Moutafis, N. Reyren, J. Sampaio, C. Vaz, N. Van Horne, K. Bouzehouane, K. Garcia, C. Deranlot, and P. Warnicke, Additive interfacial chiral interaction in

multilayers for stabilization of small individual skyrmions at room temperature, Nat. Nanotechnol. **11**, 444 (2016).

[31] A. Soumyanarayanan, M. Raju, A. Gonzalez Oyarce, A. K. Tan, M.-Y. Im, A. P. Petrović, P. Ho, K. Khoo, M. Tran, and C. Gan, Tunable room-temperature magnetic skyrmions in Ir/Fe/Co/Pt multilayers, Nat. Mater. **16**, 898 (2017).

[32] K. Wang, V. Bheemarasetty, J. Duan, S. Zhou, and G. Xiao, Fundamental physics and applications of skyrmions: A review, J. Magn. Magn. Mater. **563**, 169905 (2022).

[33] I. Dzyaloshinsky, A thermodynamic theory of "weak" ferromagnetism of antiferromagnetics, J. Phys. Chem. Solids **4**, 241 (1958).

[34] T. Moriya, Anisotropic superexchange interaction and weak ferromagnetism, Phys. Rev. **120**, 91 (1960).

[35] A. Fert, V. Cros, and J. Sampaio, Skyrmions on the track, Nat. Nanotechnol. **8**, 152 (2013).

[36] K. Wang, L. Qian, S.-C. Ying, G. Xiao, and X. Wu, Controlled modification of skyrmion information in a three-terminal racetrack memory, Nanoscale **11**, 6952 (2019).

[37] J. Tang, Y. Wu, W. Wang, L. Kong, B. Lv, W. Wei, J. Zang, M. Tian, and H. Du, Magnetic skyrmion bundles and their current-driven dynamics, Nat. Nanotechnol. **16**, 1086 (2021).

[38] W. Wang, D. Song, W. Wei, P. Nan, S. Zhang, B. Ge, M. Tian, J. Zang, and H. Du, Electrical manipulation of skyrmions in a chiral magnet, Nat. Commun. **13**, 1593 (2022).

[39] X. Zhang, M. Ezawa, and Y. Zhou, Magnetic skyrmion logic gates: conversion, duplication and merging of skyrmions, Sci. Rep. **5**, 9400 (2015).

[40] Z. Yan, Y. Liu, Y. Guang, K. Yue, J. Feng, R. Lake, G. Yu, and X. Han, Skyrmion-based programmable logic device with complete boolean logic functions, Phys. Rev. Appl. **15**, 064004 (2021).

[41] K. Raab, M. A. Brems, G. Beneke, T. Dohi, J. Rothörl, F. Kammerbauer, J. H. Mentink, and M. Kläui, Brownian reservoir computing realized using geometrically confined skyrmion dynamics, Nat. Commun. **13**, 6982 (2022).

[42] J. Zázvorka, F. Jakobs, D. Heinze, N. Keil, S. Kromin, S. Jaiswal, K. Litzius, G. Jakob, P. Virnau, and D. Pinna, Thermal skyrmion diffusion used in a reshuffler device, Nat. Nanotechnol. **14**, 658 (2019).

[43] Y. Jibiki, M. Goto, E. Tamura, J. Cho, S. Miki, R. Ishikawa, H. Nomura, T. Srivastava, W. Lim, and S. Auffret, Skyrmion Brownian circuit implemented in continuous ferromagnetic thin film, Appl. Phys. Lett. **117**, 082402 (2020).

[44] R. Ishikawa, M. Goto, H. Nomura, and Y. Suzuki, Implementation of skyrmion cellular automaton using Brownian motion and magnetic dipole interaction, Appl. Phys. Lett. **119**, 072402 (2021).

[45] K. Wang, Y. Zhang, V. Bheemarasetty, S. Zhou, S.-C. Ying, and G. Xiao, Single skyrmion true random number generator using local dynamics and interaction between skyrmions, Nat. Commun. **13**, 722 (2022).

[46] K. M. Song, J.-S. Jeong, B. Pan, X. Zhang, J. Xia, S. Cha, T.-E. Park, K. Kim, S. Finizio, and J. Raabe, Skyrmion-based artificial synapses for neuromorphic computing, Nat. Electron. **3**, 148 (2020).

[47] C. Reichhardt and C. O. Reichhardt, Noise fluctuations and drive dependence of the skyrmion Hall effect in disordered systems, New J. Phys. **18**, 095005 (2016).

[48] R. Gruber, J. Zázvorka, M. A. Brems, D. R. Rodrigues, T. Dohi, N. Kerber, B. Seng, M. Vafaee, K. Everschor-Sitte, and P. Virnau, Skyrmion pinning energetics in thin film systems, Nat. Commun. **13**, 3144 (2022).

[49] K. Litzius, J. Leliaert, P. Bassirian, D. Rodrigues, S. Kromin, I. Lemesh, J. Zazvorka, K.-J. Lee, J. Mulkers, and N. Kerber, The role of temperature and drive current in skyrmion dynamics, Nat. Electron. **3**, 30 (2020).

[50] X. Zhang, N. Vernier, W. Zhao, H. Yu, L. Vila, Y. Zhang, and D. Ravelosona, Direct observation of domain-wall surface tension by deflating or inflating a magnetic bubble, Phys. Rev. Appl. **9**, 024032 (2018).

[51] S. Lemerle, J. Ferré, C. Chappert, V. Mathet, T. Giamarchi, and P. Le Doussal, Domain wall creep in an Ising ultrathin magnetic film, Phys. Rev. Lett. **80**, 849 (1998).

[52] See Supplemental Material at [URL will be inserted by publisher] for details on sample fabrication, experimental setup, magnetic properties of the magnetic multilayer, evidence of skyrmions and their manipulations, effects of the sputtering rate on the pinning of magnetic structures, and additional simulation and experimental results.

[53] H. Yang, M. Chshiev, B. Dieny, J. Lee, A. Manchon, and K. Shin, First-principles investigation of the very large perpendicular magnetic anisotropy at Fe| MgO and Co| MgO interfaces, Phys. Rev. B **84**, 054401 (2011).

[54] B. Dieny and M. Chshiev, Perpendicular magnetic anisotropy at transition metal/oxide interfaces and applications, Rev. Mod. Phys. **89**, 025008 (2017).

[55] G. Yu, P. Upadhyaya, Y. Fan, J. G. Alzate, W. Jiang, K. L. Wong, S. Takei, S. A. Bender, L.-T. Chang, and Y. Jiang, Switching of perpendicular magnetization by spin–orbit torques in the absence of external magnetic fields, Nat. Nanotechnol. **9**, 548 (2014).

[56] B. Rodmacq, A. Manchon, C. Ducruet, S. Auffret, and B. Dieny, Influence of thermal annealing on the perpendicular magnetic anisotropy of Pt/Co/AlOx trilayers, Phys. Rev. B **79**, 024423 (2009).

[57] M. Xu, M. Li, P. Khanal, A. Habiboglu, B. Insana, Y. Xiong, T. Peterson, J. C. Myers, D. Ortega, and H. Qu, Voltage-controlled antiferromagnetism in magnetic tunnel junctions, Phys. Rev. Lett. **124**, 187701 (2020).

[58] Y. Fan, K. Smith, G. Lüpke, A. Hanbicki, R. Goswami, C. Li, H. Zhao, and B. Jonker, Exchange bias of the interface spin system at the Fe/MgO interface, Nat. Nanotechnol. **8**, 438 (2013).

[59] L. Qian, K. Wang, Y. Zheng, and G. Xiao, Spin Hall effect in the α and β phases of T a x W 1− x alloys, Phys. Rev. B **102**, 094438 (2020).

[60] R. L. Conte, E. Martinez, A. Hrabec, A. Lamperti, T. Schulz, L. Nasi, L. Lazzarini, R. Mantovan, F. Maccherozzi, and S. Dhesi, Role of B diffusion in the interfacial Dzyaloshinskii-Moriya interaction in Ta/Co 20 F e 60 B 20/MgO nanowires, Phys. Rev. B **91**, 014433 (2015).

[61] M. Cecot, Ł. Karwacki, W. Skowroński, J. Kanak, J. Wrona, A. Żywczak, L. Yao, S. van Dijken, J. Barnaś, and T. Stobiecki, Influence of intermixing at the Ta/CoFeB interface on spin Hall angle in Ta/CoFeB/MgO heterostructures, Sci. Rep. **7**, 968 (2017).

[62] J. J. Senkevich, T. Karabacak, D.-L. Bae, and T. S. Cale, Formation of body-centered-cubic tantalum via sputtering on low-κ dielectrics at low temperatures, J. Vac. Sci. Technol. **24**, 534 (2006).

[63] H. Zhang, S. Yamamoto, Y. Fukaya, M. Maekawa, H. Li, A. Kawasuso, T. Seki, E. Saitoh, and K. Takanashi, Current-induced spin polarization on metal surfaces probed by spin-polarized positron beam, Sci. Rep. **4**, 4844 (2014).

[64] J. J. Colin, G. Abadias, A. Michel, and C. Jaouen, On the origin of the metastable β-Ta phase stabilization in tantalum sputtered thin films, Acta Mater. **126**, 481 (2017).

[65] E. A. Ellis, M. Chmielus, and S. P. Baker, Effect of sputter pressure on Ta thin films: Beta phase formation, texture, and stresses, Acta Mater. **150**, 317 (2018).

[66] S. Sato, T. Inoue, and H. Sasaki, Thermal oxidation of β-Ta below 500° C, Thin Solid Films **86**, 21 (1981).

[67] Q. Hao, W. Chen, and G. Xiao, Beta (β) tungsten thin films: Structure, electron transport, and giant spin Hall effect, Appl. Phys. Lett. **106**, 182403 (2015).

[68] A. Patterson, The Scherrer formula for X-ray particle size determination, Phys. Rev. **56**, 978 (1939).

[69] E. Zubler, The gettering properties of tantalum, J. Electrochem. Soc. **110**, 1072 (1963).

[70] Y. A. Vodakov, A. Roenkov, M. Ramm, E. Mokhov, and Y. N. Makarov, Use of Ta- container for sublimation growth and doping of SiC bulk crystals and epitaxial layers, Phys. Status Solidi B **202**, 177 (1997).

[71] T. F. K. Lilov, S. O. S. Ohshima, and S. N. S. Nishino, Effect of tantalum in crystal growth of silicon carbide by sublimation close space technique, Jpn. J. Appl. Phys. **40**, 6737 (2001).

[72] E. Krikorian and R. Sneed, Deposition of tantalum, tantalum oxide, and tantalum nitride with controlled electrical characteristics, J. Appl. Phys. **37**, 3674 (1966).

[73] L. Feinstein and R. Huttemann, Factors controlling the structure of sputtered Ta films, Thin Solid Films **16**, 129 (1973).

[74] R. Knepper, B. Stevens, and S. P. Baker, Effect of oxygen on the thermomechanical behavior of tantalum thin films during the β–α phase transformation, J. Appl. Phys. **100**, 123508 (2006).

[75] T. Meier, M. Kronseder, and C. Back, Domain-width model for perpendicularly magnetized systems with Dzyaloshinskii-Moriya interaction, Phys. Rev. B **96**, 144408 (2017).

[76] I. Lemesh, F. Büttner, and G. S. Beach, Accurate model of the stripe domain phase of perpendicularly magnetized multilayers, Phys. Rev. B **95**, 174423 (2017).

[77] A. B. Kolton, A. Rosso, T. Giamarchi, and W. Krauth, Creep dynamics of elastic manifolds via exact transition pathways, Phys. Rev. B **79**, 184207 (2009).

[78] V. Jeudy, A. Mougin, S. Bustingorry, W. S. Torres, J. Gorchon, A. B. Kolton, A. Lemaître, and J.-P. Jamet, Universal pinning energy barrier for driven domain walls in thin ferromagnetic films, Phys. Rev. Lett. **117**, 057201 (2016).

[79] K. Shahbazi, J.-V. Kim, H. T. Nembach, J. M. Shaw, A. Bischof, M. D. Rossell, V. Jeudy, T. A. Moore, and C. H. Marrows, Domain-wall motion and interfacial Dzyaloshinskii-Moriya interactions in Pt/Co/Ir (t Ir)/Ta multilayers, Phys. Rev. B **99**, 094409 (2019).

[80] W. S. Torres, R. D. Pardo, S. Bustingorry, A. B. Kolton, A. Lemaitre, and V. Jeudy, Universal dimensional crossover of domain wall dynamics in ferromagnetic films, Phys. Rev. B **99**, 201201 (2019).

[81] M. Sampietro, L. Fasoli, and G. Ferrari, Spectrum analyzer with noise reduction by cross-correlation technique on two channels, Rev. Sci. Instrum. **70**, 2520 (1999).

[82] K. Wang, Y. Zhang, and G. Xiao, Anomalous Hall sensors with high sensitivity and stability based on interlayer exchange-coupled magnetic thin films, Phys. Rev. Appl. **13**, 064009 (2020).

[83] Y. Zhang, K. Wang, and G. Xiao, Noise characterization of ultrasensitive anomalous Hall effect sensors based on Co40Fe40B20 thin films with compensated in-plane and perpendicular magnetic anisotropies, Appl. Phys. Lett. **116**, 212404 (2020).

[84] K. Wang, Y. Zhang, S. Zhou, and G. Xiao, Micron-Scale Anomalous Hall Sensors Based on Fe x Pt1− x Thin Films with a Large Hall Angle and near the Spin-Reorientation Transition, Nanomaterials **11**, 854 (2021).

[85] N. Nagaosa, J. Sinova, S. Onoda, A. H. MacDonald, and N. P. Ong, Anomalous hall effect, Rev. Mod. Phys. **82**, 1539 (2010).

[86] L. Liu, C.-F. Pai, Y. Li, H. Tseng, D. Ralph, and R. Buhrman, Spin-torque switching with the giant spin Hall effect of tantalum, Science **336**, 555 (2012).

[87] Q. Hao and G. Xiao, Giant spin Hall effect and magnetotransport in a Ta/CoFeB/MgO layered structure: A temperature dependence study, Phys. Rev. B **91**, 224413 (2015).

[88] K. Wang, L. Qian, W. Chen, S.-C. Ying, G. Xiao, and X. Wu, Spin torque effect on topological defects and transitions of magnetic domain phases in Ta/CoFeB/MgO, Phys. Rev. B **99**, 184410 (2019).

[89] S.-Z. Lin, C. Reichhardt, C. D. Batista, and A. Saxena, Particle model for skyrmions in metallic chiral magnets: Dynamics, pinning, and creep, Phys. Rev. B **87**, 214419 (2013).

[90] O. I. Utesov, Thermodynamically stable skyrmion lattice in a tetragonal frustrated antiferromagnet with dipolar interaction, Phys. Rev. B **103**, 064414 (2021).

[91] C. Song, N. Kerber, J. Rothörl, Y. Ge, K. Raab, B. Seng, M. A. Brems, F. Dittrich, R. M. Reeve, and J. Wang, Commensurability between element symmetry and the number of skyrmions governing skyrmion diffusion in confined geometries, Adv. Funct. Mater. **31**, 2010739 (2021).

[92] A. Vansteenkiste, J. Leliaert, M. Dvornik, M. Helsen, F. Garcia-Sanchez, and B. Van Waeyenberge, The design and verification of MuMax3, AIP advances **4**, 107133 (2014).

[93] A. Gurevich, Distribution of pinning energies and the resistive transition in superconducting films, Phys. Rev. B **42**, 4857 (1990).

[94] S. Demirdiş, C. J. van der Beek, Y. Fasano, N. R. Cejas Bolecek, H. Pastoriza, D. Colson, and F. Rullier-Albenque, Strong pinning and vortex energy distributions in single-crystalline Ba(Fe${}_{1\ensuremath{-}x}$Co${}_{x}$)${}_{2}$As${}_{2}$, Phys. Rev. B **84**, 094517 (2011).

[95] V. Sandu, A. M. Ionescu, G. Aldica, M. A. Grigoroscuta, M. Burdusel, and P. Badica, On the pinning force in high density MgB2 samples, Sci. Rep. **11**, 5951 (2021).

[96] X. Wang, H. Yuan, and X. Wang, A theory on skyrmion size, Commun. Phys. **1**, 31 (2018).

[97] D. Maccariello, W. Legrand, N. Reyren, K. Garcia, K. Bouzehouane, S. Collin, V. Cros, and A. Fert, Electrical detection of single magnetic skyrmions in metallic multilayers at room temperature, Nat. Nanotechnol. **13**, 233 (2018).

[98] L. Desplat and J.-V. Kim, Entropy-reduced retention times in magnetic memory elements: a case of the Meyer-Neldel compensation rule, Phys. Rev. Lett. **125**, 107201 (2020).

[99] L. Desplat, C. Vogler, J.-V. Kim, R. L. Stamps, and D. Suess, Path sampling for lifetimes of metastable magnetic skyrmions and direct comparison with Kramers' method, Phys. Rev. B **101**, 060403 (2020).

[100] L. Desplat and J.-V. Kim, Quantifying the thermal stability in perpendicularly magnetized ferromagnetic nanodisks with forward flux sampling, Phys. Rev. Appl. **14**, 064064 (2020).